Zhao *et al.*
Chinese Journal of Mechanical Engineering (2024) 37:75
https://doi.org/10.1186/s10033-024-01049-x

Chinese Journal of Mechanical Engineering

ORIGINAL ARTICLE

Open Access

Vibration Reduction by a Partitioned Dynamic Vibration Absorber with Acoustic Black Hole Features

Xiaoning Zhao[1], Chaoyan Wang[1,2], Hongli Ji[1*], Jinhao Qiu[1] and Li Cheng[3]

Abstract

Vibration quality is a vital indicator for assessing the progress of modern equipment. The dynamic vibration absorber (DVA) based on the acoustic black hole (ABH) feature is a new passive control method that manipulates waves. It offers efficient energy focalization and broad-spectrum vibration suppression, making it highly promising for applications in large equipment such as aircraft, trains, and ships. Despite previous advancements in ABH-DVA development, certain challenges remain, particularly in ensuring effective coupling with host structures during control. To address these issues, this study proposes a partitioned ABH-featured dynamic vibration absorber (PABH-DVA) with partitions in the radial direction of the disc. By employing a plate as the host structure, simulations and experiments were conducted, demonstrating that the PABH-DVA outperforms the original symmetric ABH-DVA in terms of damping performance. The study also calculated and compared the coupling coefficients of the two ABH-DVAs to uncover the mechanism behind the enhanced damping. Simulation results revealed that the PABH-DVA exhibits more coupled modes, occasionally with lower coupling coefficients than the symmetric ABH-DVA. The influence of frequency ratio and modal mass was further analyzed to explain the reasons behind the PABH-DVA's superior damping performance. Additionally, the study discussed the impact of the number of slits and their orientation. This research further explains the coupling mechanism between the ABH-DVA and the controlled structure, and provides new ideas for the further application of ABH in engineering.

Keywords Acoustic black hole, Vibration control, Dynamic vibration absorber, Coupling analysis

1 Introduction

Vibration reduction is a crucial issue that must be considered for many equipment devices [1, 2]. As a passive damping technique, acoustic black hole (ABH) structure has a great prospect for vibration and noise control due to its wide applicable frequency range, light-weight as well as simple and flexible implementation [3]. In one-dimensional cases, an ABH structure is wedge-shaped, with its thickness varying according to a power-law function. When bending waves propagate to the conical tip, their phase velocity gradually decreases to zero, resulting in zero reflection, theoretically [4]. In two-dimensional cases, a similar occurrence can result in the formation of a lens that can focus the wave energy at a specific location [5]. By using a small amount of damping substance at the ABH region's thinnest area, the bending waves can be effectively slowed down, concentrated and finally dissipated. This process can be used to suppress structural vibration, which makes it possible for prospective engineering applications.

*Correspondence:
Hongli Ji
jihongli@nuaa.edu.cn
[1] State Key Laboratory of Mechanics and Control of Mechanical Structures, Nanjing University of Aeronautics and Astronautics, Nanjing 210016, China
[2] Nanjing Institute of Information Technology, Nanjing 210016, China
[3] Department of mechanical Engineering, Hong Kong Polytechnic University, Kowloon 999077, Hong Kong, China

Existing researches on ABH are grooming in the past few decades, including many aspects such as theoretical analyses [3–8], experimental researches [9–12], structural design [13–17], optimization [18–20] and some burgeoning engineering applications such as vibration and noise reduction and energy recovery [21–25]. The most recent evaluations of the state-of-the-art in ABH research as well as some prospective applications were provided by Pelat et al. [26] and Zhao et al. [27]. However, in the majority of the above researches, ABH is embedded into a structure via thinning thickness. Though lightweight, such ABH structure suffers from compromised structural stiffness and strength, which hinders its use when certain load-bearing capability is required.

Recently, the concept of add-on ABH-featured dynamic vibration dampers was proposed for broadband vibration suppression [28]. The working principle embraces the advantages of both dynamic vibration absorbers and waveguide absorbers [28–32]. Early adoption of ABH principle in a DVA structure is a 1D resonant beam damper proposed by Zhou et al. [28], followed by more sophisticated designs such as ABH-based circular and eccentric dynamic vibration absorber by Ji et al. [29, 30], a planar swirl-shaped ABH absorber by Zhou et al. [31], and a spiral ABH waveguide absorber by Park et al. [32]. It is worth mentioning that Ji et al. proposed the symmetric [29] and eccentric [30] dynamic vibration absorbers based on two-dimensional ABH (2D SABH-DVA and EABH-DVA) to deal with multi-directional flexural waves. These studies demonstrated that only a few modes of the symmetrical vibration absorber can be coupled with the host structure; the selective coupling mode hinders the vibration suppression ability of the device, a problem which can be tackled to some extent by an eccentric design. In Ref. [30], the coupling coefficient is defined to evaluate the coupling effect between the host structure and add-on structure. However, the above studies are only limited to discussing the influence of modal shape on the coupling effect. Effects of other factors involved in the coupling such as modal vector, frequency ratio, mass matrix and installation angle, remain unknown.

To tackle the aforementioned problem, a new partitioned ABH-based dynamic vibration absorber (abbreviated as PABH-DVA) is proposed as an auxiliary add-on device for the vibration reduction of a vibrating structure under control. The proposed configuration retains the basic ABH profile with partitions along the radial direction of the disc, thus preserving the energy focalization characteristics at each cut segment. Both simulation and experimental results show that, breaking its structural symmetry, the proposed PABH-DVA not only improves the coupling with the host structure, but also increases the modal density of the add-on ABH structure owing to the cutting slits to enhance the chance of coupling with the vibration modes of the host structure, so as to improve the vibration suppression performance. The slot position of the add-on ABH structure does not need particular optimization, while the traditional passive DVA damper often needs meticulous adjustment to achieve good control results. To revealing the damping mechanism by the PABH-DVA, the influence of the frequency ratio between a mode of the DVA and that of the host structure is considered. Mathematical expressions of the resonance frequencies and the modal amplitude at the two resonance peaks of the coupled system are derived. Numerical examples are conducted for typical values of the frequency ratio and coupling coefficient. To consider the influence of mass ratio, modal participation factor and effective modal mass, which are closed related to the coupling coefficient, are introduced. The effective modal mass proportion and the accumulative modal mass proportion of the PABH-DVA are calculated and compared with those of the SABH-DVA. The influence of the number of slits and the installation angle is also investigated. Both the simulation results and experimental results show that the PABH-DVA outperforms the SABH-DVA in terms of vibration suppression performance.

A partitioned ABH-based dynamic vibration absorber (PABH-DVA) is proposed in this paper to address the problem of selective coupling encountered in traditional ABH-DVA for vibration reduction. To analyze the vibration suppression mechanism of the PABH-DVA and clarify the mass effect in coupling, the frequency ratio is defined. The study also investigates the influence of the number of slits and the installation angle. The findings demonstrate that achieving a large coupling coefficient and an appropriate frequency ratio are crucial prerequisites for achieving effective vibration suppression.

The paper is organized as follows: Section 1 provides an introduction to the study's focus. Section 2 presents the geometry, vibration damping performance, and coupling analysis of the PABH-DVA. In Section 3, the mechanism behind the enhanced damping effect is discussed. Section 4 examines the influencing factors, including the number of slits and the installation angle. Experimental results are presented in Section 5, and finally, Section 6 summarizes the conclusions. The research flowchart of this article is shown in Figure 1.

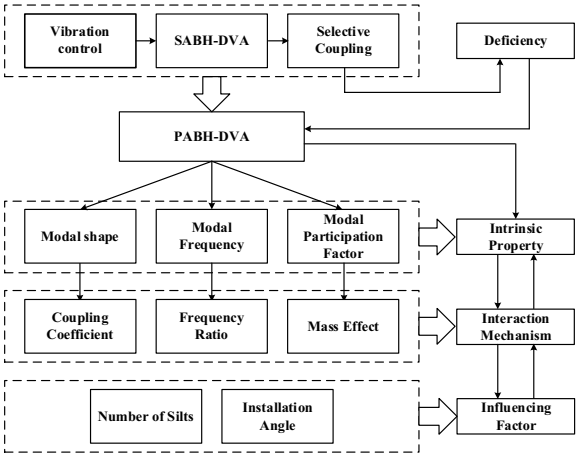

Figure 1 Flow diagram of the research

2 PABH-DVA and Its Vibration Damping Performance

2.1 Geometry of the PABH-DVA

The symmetrical configuration of the SABH-DVA is shown in Figure 2. It contains three parts: A uniform central plateau with a constant thickness h_0 (from 0 to r_1), an annular domain with a varying thickness (from r_1 to r_2) and an annular platform with uniform thickness h_1 (from r_2 to r_3). The thickness variation along the radial direction is as follows:

$$h(r) = \begin{cases} h_0, & (0 \le r \le r_1), \\ \varepsilon(r - r_2)^m + h_1, & (r_1 \le r \le r_2), \\ h_1, & (r_2 \le r \le r_3), \end{cases} \tag{1}$$

where ε is the multiplier of the ABH curve, which determined by radius and maximum thickness, m is the power index of the ABH curve.

An annular damping layer of a constant thickness h_d is bonded along its outer edge of the ABH-featured disk, as shown in Figure 2(b). The above disc is radially partitioned through cutting a seam width d in the area except the center of ABH disk by mechanical cutting method. Since there are many partition schemes to choose, a DVA partitioned into three parts is taken as an example, as shown in Figure 2(c), abbreviated as P3ABH-DVA.

The P3ABH-DVA is attached to a host structure, exemplified by a rectangular plate, using either glue or a bolt,

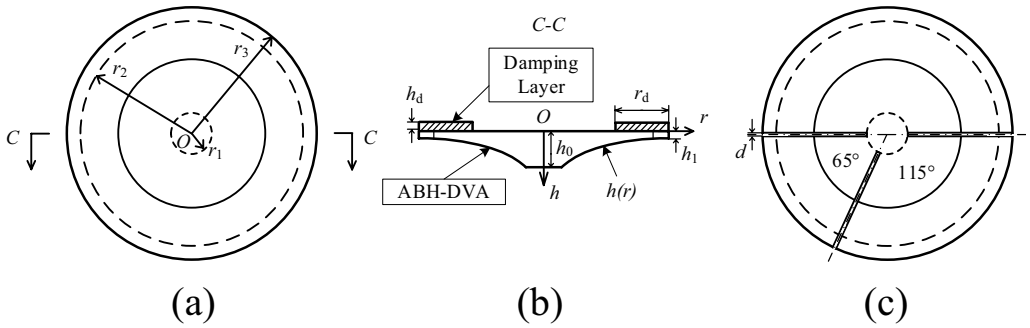

Figure 2 Schematic of a 2D symmetric and partitioned ABH-DVA: (**a**) Vertical view of SABH-DVA, (**b**) Main view of SABH-DVA, (**c**) Vertical view of P3ABH-DVA

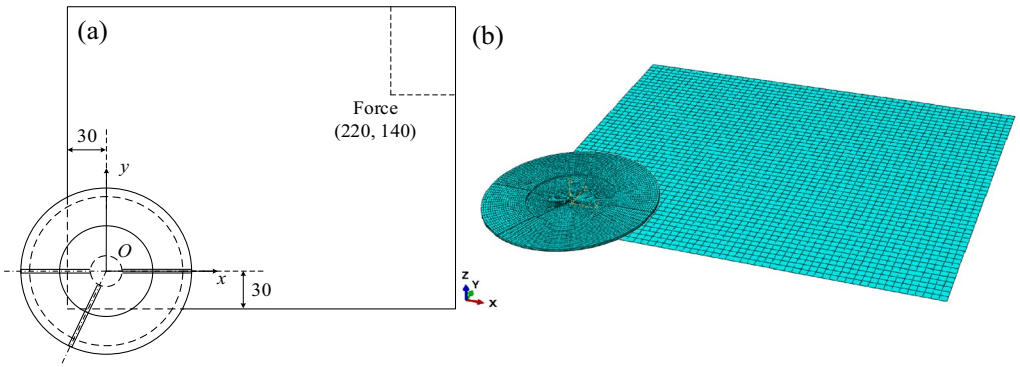

Figure 3 Synthesized system containing a host plate and an add-on DVA device: (**a**) Synthesis system, (**b**) Finite element model

Table 1 Material parameters

	Aluminum	Damping
Young's modulus (MPa)	70000	200
Poisson's ratio	0.346	0.45
Density (kg·m^{-3})	2710	1850
Material loss factor	0.001	0.1

Table 2 Structural geometric parameters

Parameters (mm)	Value
ε	0.00112
m	2
r_1	5
r_2	55
r_3	61
h_0	3
h_1	0.2
h_d	2
r_4	30
d	1

as shown in Figure 3(a). As an add-on device, rather than an embedded indentation into the host structure, its inclusion does not jeopardize the stiffness or the mechanical strength of the host structure.

For numerical analyses, aluminum serves as the primary material for the PABH-DVA and the host structure, while butyl rubber serves as the damping substance. The dimension of the host structure measures 300 mm × 240 mm × 6 mm in the present case, the total mass of the P3ABH-DVA is set to 0.0521 kg, which is 4.45% of the host plate. The P3ABH-DVA is installed at a position 30 mm away from both sides of the plate, and this point is used as the origin of the coordinate system, as shown in Figure 3(a). The plate is excited by a transverse force of 1 N in amplitude at a point with a coordinate of (220, 140) mm. It should be mentioned that the position of the installation is not optimized in this case. Because most of the modes of a plate with free boundaries have considerable vibration amplitude in the corners, it was decided to install close to one of the plate's corners, so as to expect that the PABH-DVA can still couple with as many modes as possible within the given and broad frequency range. As shown in Ref. [30], the large vibration amplitude in the three degrees of freedom (one translational and two rotational) of the installation point warrants good coupling between the ABH-DVA and the host structure. The material and geometrical parameters of the host structure and those of the ABH-DVAs are listed in Tables 1 and 2, respectively.

Numerical simulations are performed using Abaqus to gain insights into the dynamics of the host structure, add-on devices, and their synthetic systems. The host structure is represented using shell elements (S8R), while the add-on DVA is modeled using 3D solid elements (C3D20R), as depicted in Figure 3(b). Refined grids are utilized in the margins of the P3ABH-DVA and SABH-DVA to ensure the accuracy of the numerical simulations. The mesh size is chosen to ensure a minimum of ten elements per wavelength. For modal analysis, both the host structure and the synthetic systems are subjected to free boundary conditions. A rigid connection is applied over the installation interface, which refers to the central plateau of the add-on DVAs.

The driving point mobility v_{dp} and mean velocity of the plate $\langle v_n \rangle$, normalized based on exciting force, with a reference value of 1 m·s^{-1}·N^{-1}, are defined to evaluate the vibration level of the plate, the mean velocity $\langle v_n \rangle$ can be defined as:

$$\langle v_n \rangle = \frac{1}{S} \int |v_n| \mathrm{d}S, \tag{2}$$

where v_n is the normal velocity of the plate and S is the whole vibrating surface. Using the logarithmic value of the normalized speed according to the excitation force as the vibration level.

2.2 Vibration Damping Performance of the P3ABH-DVA

Figure 4(a) illustrates the driving point mobility of the uniform plate, along with the synthetic system incorporating both the P3ABH-DVA and SABH-DVA of equal size. It is evident that the addition of DVAs effectively suppresses structural vibrations in the system. Furthermore, the P3ABH-DVA exhibits a better performance than the SABH-DVA in terms of reducing specific peaks, particularly at frequencies of 218 Hz, 640 Hz, 967 Hz, and 1962 Hz. At these frequencies, attenuation levels of 10 dB, 19 dB, 15 dB, and 25 dB are achieved, respectively. However, for most peaks, there is not a significant difference between the two DVAs. The mean velocity of the host plate follows a similar trend, as depicted in Figure 4(b). In other words, the P3ABH-DVA provides additional vibration reduction at certain frequencies that can also be addressed by the SABH-DVA.

Further inspection of the response curve suggests two main vibration suppression phenomena: The dynamic interaction (conventional DVA effect) evidenced by the typical peak splitting phenomenon; and damping enhancement (energy dissipation) as reflected by the reduction in some resonance peaks without splitting, in agreement with previous observations made in SABH-DVA [29] and EABH-DVA cases [30].

Although both the previously proposed EABH-DVA and PABH-DVA can improve the selective coupling of the SABH-DVA, differences exist between them in terms of physical mechanism. The former changes the modal distribution without changing the effective modal mass and

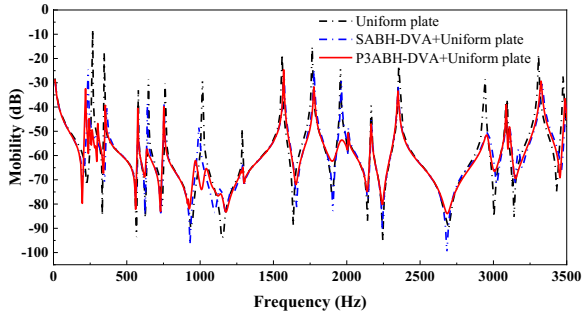

(a) Driving point mobility

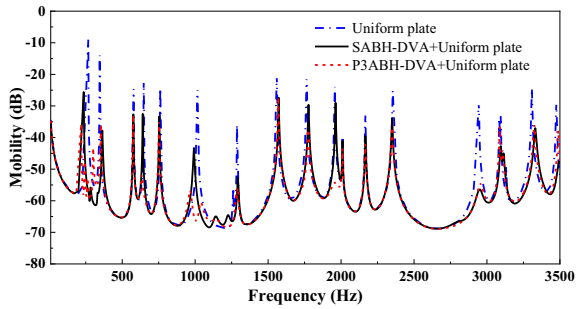

(b) Mean velocity

Figure 4 Driving point mobility of the host plate with different add-on DVAs

modal density, while the latter increases the modal density (to be confirmed in Section 3.1) by sacrificing a small amount of effective modal mass (to be confirmed in Section 3.2) to achieve the above purpose. But in aggregate, the occurrence of the aforementioned phenomena would both rely on an effective dynamic coupling between the host structure and the add-on ABH-DVA, which calls for further analyses in the later section.

2.3 Coupling Analyses through Coupling Coefficients

The coupling coefficients between the modes of the add-on DVA and those of the host structure have been used to evaluate the coupling characteristics of the two coupled sub-structures [30]. For completeness and convenience of later usage, the formulation of the coupling coefficient is briefly recalled. The dynamic equation of each sub-discretized system has the following form:

$$\boldsymbol{M}_{\mathrm{A}}\ddot{\boldsymbol{w}}_{\mathrm{A}}+\boldsymbol{C}_{\mathrm{A}}\dot{\boldsymbol{w}}_{\mathrm{A}}+\boldsymbol{K}_{\mathrm{A}}\boldsymbol{w}_{\mathrm{A}}=0, \tag{3}$$

$$\boldsymbol{M}_{\mathrm{s}}\ddot{\boldsymbol{w}}_{\mathrm{s}}+\boldsymbol{C}_{\mathrm{s}}\dot{\boldsymbol{w}}_{\mathrm{s}}+\boldsymbol{K}_{\mathrm{s}}\boldsymbol{w}_{\mathrm{s}}=\boldsymbol{F}, \tag{4}$$

where $\boldsymbol{M}_{\mathrm{A}}$, $\boldsymbol{C}_{\mathrm{A}}$ and $\boldsymbol{K}_{\mathrm{A}}$ are the mass, damping and stiffness matrices for the add-on DVA, $\boldsymbol{M}_{\mathbf{s}}$, $\boldsymbol{C}_{\mathbf{s}}$ and $\boldsymbol{K}_{\mathbf{s}}$ are those for the host structure; $\boldsymbol{w}_{\mathrm{A}}$ and $\boldsymbol{w}_{\mathrm{s}}$ are their corresponding nodal displacements; $\boldsymbol{F}$ is the excitation force acting on the host structure.

Using the modal superposition method and normalizing according to the modal mass, Eqs. (3) and (4) can be written as the following form in the principal coordinates as:

$$\boldsymbol{I}\ddot{\boldsymbol{q}}_{\mathrm{A}}+[2\omega_{\mathrm{A}}\zeta_{\mathrm{A}}]\dot{\boldsymbol{q}}_{\mathrm{A}}+\left[\omega_{\mathrm{A}}^2\right]\boldsymbol{q}_{\mathrm{A}}=0, \tag{5}$$

$$\boldsymbol{I}\ddot{\boldsymbol{q}}_{\mathrm{s}}+[2\omega_{\mathrm{s}}\zeta_{\mathrm{s}}]\dot{\boldsymbol{q}}_{\mathrm{s}}+\left[\omega_{\mathrm{s}}^2\right]\boldsymbol{q}_{\mathrm{s}}=\boldsymbol{F}_{\mathrm{m}}, \tag{6}$$

where $\boldsymbol{I}$ is a unit matrix, $\boldsymbol{q}_{\mathrm{A}}$ is the modal coordinate of the add-on DVA; $[2\omega_{\mathrm{A}}\zeta_{\mathrm{A}}]$ is a diagonal matrix with its ith diagonal element equal to $2\omega_{\mathrm{A}i}\zeta_{\mathrm{A}}$, where $\omega_{\mathrm{A}i}$ and ζ_{A} are the natural frequency and the modal damping ratio of the add-on DVA respectively. $[\omega_{\mathrm{A}}^2]$ is also a diagonal matrix and its non-zero diagonal elements are $\omega_{\mathrm{A}i}^2$. Replacing sub-index A by s, all quantities apply to the host structure.

According to the previous definition [30], the displacement of the add-on DVA attached to the nth node of the host structure can be written as:

$$\boldsymbol{w}_{\mathrm{A}}=\boldsymbol{\Phi}_{\mathrm{A}}\boldsymbol{q}_{\mathrm{A}}+\{1\}w_{\mathrm{s}n}+\boldsymbol{R}_y\theta_{nx}+\boldsymbol{R}_x\theta_{ny}, \tag{7}$$

where $\boldsymbol{\Phi}_{\mathrm{A}}$ is the modal shape matrix of the add-on DVA, $\{1\}$, $\boldsymbol{R}_y$, $\boldsymbol{R}_x$ are $N_{\mathrm{A}}\times1$ vectors, and their components are all equal to 1, y coordinate and x coordinate of the corresponding node, respectively. $w_{\mathrm{s}n}$, θ_{nx} and θ_{ny} are the out-of-plane displacement and the two rotational angles, respectively.

Substituting Eq. (7) into Eq. (3) and utilizing Eqs. (5) and (6) give:

$$\begin{aligned}&\boldsymbol{I}\ddot{\boldsymbol{q}}_{\mathrm{A}}+\boldsymbol{\Phi}_{\mathrm{A}}^{\mathrm{T}}\boldsymbol{M}_{\mathrm{A}}\left(\{1\}\boldsymbol{G}_1+\boldsymbol{R}_y\boldsymbol{G}_2+\boldsymbol{R}_x\boldsymbol{G}_3\right)\boldsymbol{\Phi}_{\mathrm{s}}\ddot{\boldsymbol{q}}_{\mathrm{s}}\\&+[2\omega_{\mathrm{A}}\zeta_{\mathrm{A}}]\dot{\boldsymbol{q}}_{\mathrm{A}}+\left[\omega_{\mathrm{A}}^2\right]\boldsymbol{q}_{\mathrm{A}}=0,\end{aligned} \tag{8}$$

$$\begin{aligned}&\boldsymbol{I}\ddot{\boldsymbol{q}}_s+\boldsymbol{\Phi}_s^{\mathrm{T}}\left(\boldsymbol{G}_1^{\mathrm{T}}\{1\}^{\mathrm{T}}+\boldsymbol{G}_2^{\mathrm{T}}\boldsymbol{R}_y^{\mathrm{T}}+\boldsymbol{G}_3^{\mathrm{T}}\boldsymbol{R}_x^{\mathrm{T}}\right)\boldsymbol{M}_A\boldsymbol{\Phi}_A\ddot{\boldsymbol{q}}_A\\&+[2\omega_s\zeta_s]\dot{\boldsymbol{q}}_s+\left[\omega_s^2\right]\boldsymbol{q}_s=\boldsymbol{F}_{\mathrm{m}}.\end{aligned} \tag{9}$$

Obviously, the second term in the aforementioned equations determines the coupling between the add-on DVA and the host structure. According to Eqs. (8), (9), the coupling coefficient between the ith mode of the add-on DVA and the jth mode of the host structure, denoted by α_{ij}, can be defined as:

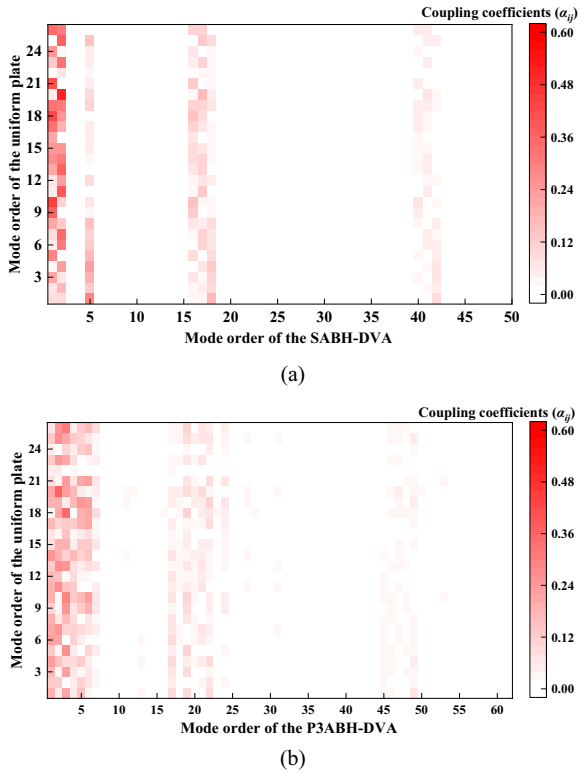

Figure 5 Modal coupling coefficients between the two types of add-on DVAs and the host structure within 3500 Hz: (**a**) SABH-DVA, (**b**) P3ABH-DVA

$$\begin{aligned}\alpha_{ij} &= \boldsymbol{\Phi}_{\mathrm{A}i}^{\mathrm{T}}\left(\boldsymbol{M}_{\mathrm{A}}\{1\}\boldsymbol{G}_1 + \boldsymbol{M}_{\mathrm{A}}\boldsymbol{R}_y\boldsymbol{G}_2 + \boldsymbol{M}_{\mathrm{A}}\boldsymbol{R}_x\boldsymbol{G}_3\right)\boldsymbol{\Phi}_{sj} \\ &= \boldsymbol{\Phi}_{\mathrm{A}i}^{\mathrm{T}}\boldsymbol{M}_{\mathrm{A}}\{1\}\boldsymbol{G}_1\boldsymbol{\Phi}_{sj} + \boldsymbol{\Phi}_{\mathrm{A}i}^{\mathrm{T}}\boldsymbol{M}_{\mathrm{A}}\boldsymbol{R}_y\boldsymbol{G}_2\boldsymbol{\Phi}_{sj} + \boldsymbol{\Phi}_{\mathrm{A}i}^{\mathrm{T}}\boldsymbol{M}_{\mathrm{A}}\boldsymbol{R}_x\boldsymbol{G}_3\boldsymbol{\Phi}_{sj} \\ &= \alpha_{i1}^{(1)}\alpha_{j2}^{(1)} + \alpha_{i1}^{(2)}\alpha_{j2}^{(2)} + \alpha_{i1}^{(3)}\alpha_{j2}^{(3)},\end{aligned} \tag{10}$$

where

$$\begin{aligned}&\alpha_{i1}^{(1)} = \boldsymbol{\Phi}_{\mathrm{A}i}^{\mathrm{T}}\boldsymbol{M}_{\mathrm{A}}\{1\}, \quad \alpha_{i1}^{(2)} = \boldsymbol{\Phi}_{\mathrm{A}i}^{\mathrm{T}}\boldsymbol{M}_{\mathrm{A}}\boldsymbol{R}_y, \quad \alpha_{i1}^{(3)} = \boldsymbol{\Phi}_{\mathrm{A}i}^{\mathrm{T}}\boldsymbol{M}_{\mathrm{A}}\boldsymbol{R}_x, \\ &\alpha_{j2}^{(1)} = \boldsymbol{G}_1\boldsymbol{\Phi}_{sj}, \qquad \alpha_{j2}^{(2)} = \boldsymbol{G}_2\boldsymbol{\Phi}_{sj}, \qquad \alpha_{j2}^{(3)} = \boldsymbol{G}_3\boldsymbol{\Phi}_{sj}.\end{aligned} \tag{11}$$

Obviously, $\alpha_{i1}^{(k)}(k = 1, 2, 3)$ are the modal participation factors, related to the modal shapes of the add-on DVA. $\alpha_{j2}^{(k)}(k = 1, 2, 3)$ are the position vectors, determined by the installation position of the host structure.

The coupling coefficients are calculated according to Eq. (10) and Eq. (11), and the results are presented in Figure 5. It can be observed that the P3ABH-DVA exhibits coupling with the host structure for the first 6 modes, whereas the SABH-DVA only shows coupling for the 1st, 2nd, and 5th modes. Additionally, the coupling frequency band of the P3ABH-DVA is broader than that of the SABH-DVA, spanning approximately 250 Hz to 1200 Hz. This aligns with the more effective frequency band of the P3ABH-DVA demonstrated in Figure 4. It is worth noting that the modal participation factor discussed in Section 3.2 provides a similar representation, but the coupling coefficient incorporates the influence of the installation position as an additional factor.

More coupled modes in the new PABH-DVA means that it gives a greater number of dynamic dampers to the host structure. However, although there are more coupled modes in the PABH-DVA than in the original SABH-DVA, most of the coupling coefficients in the PABH-DVA are smaller than those in the SABH-DVA. Moreover, the damping effect of a dynamic damper is not only determined by the coupling coefficients, but also by its frequency ratio and mass ratio. Hence, further analysis of the mechanism for enhancing damping effect by the PABH-DVA is necessary.

3 Mechanism for Damping Effect Enhancement

3.1 Frequency Ratio

According to classical vibration theory, the frequency ratio between the mode of the DVA and the mode of the host structure plays a crucial role in achieving a good damping effect. When the damping effect is achieved, the original resonance peak of the structure splits into two, with the heights of these peaks depending on the damping ratio of the DVA. With a sufficiently high damping ratio, the two split peaks are effectively suppressed, resulting in excellent damping performance. The ideal frequency ratio is typically around 1. Deviations from this ratio lead to a deterioration in the damping effect. In the case of the ABH-DVA, each coupled mode acts as a DVA. Therefore, it becomes important to investigate the influence of the frequency ratio between the coupled mode of the ABH-DVA and that of the host structure on the damping effect.

Without loss of generality, the interaction between the *i*th mode in the add-on DVA and the *j*th mode in the host structure is considered by neglecting all the other modes. According to Eqs. (8) and (9), the equations of dynamic of the 2-DOF system become:

$$\begin{cases}\ddot{q}_{\mathrm{A}i} + \alpha_{ij}\ddot{q}_{sj} + 2\omega_{\mathrm{A}i}\zeta_{\mathrm{A}}\dot{q}_{Ai} + \omega_{\mathrm{A}i}^2 q_{\mathrm{A}i} = 0, \\ \ddot{q}_{sj} + \alpha_{ij}\ddot{q}_{\mathrm{A}i} + 2\omega_{sj}\zeta_{\mathrm{s}}\dot{q}_{sj} + \omega_{sj}^2 q_{sj} = F_{\mathrm{m}j}.\end{cases} \tag{12}$$

In the frequency domain, the equations can be expressed as:

$$\begin{bmatrix}\omega_{\mathrm{A}i}^2 - \omega^2 + j2\zeta_{\mathrm{A}}\omega_{\mathrm{A}i}\omega & -\alpha_{ij}\omega^2 \\ -\alpha_{ij}\omega^2 & \omega_{sj}^2 - \omega^2 + j2\zeta_{\mathrm{s}}\omega_{sj}\omega\end{bmatrix}\begin{Bmatrix}\tilde{q}_{\mathrm{A}i} \\ \tilde{q}_{sj}\end{Bmatrix} = \begin{Bmatrix}0 \\ \overline{F}_{\mathrm{m}j}\end{Bmatrix}, \tag{13}$$

where $\overline{F}_{\mathrm{m}j}$ is the amplitude of the modal force and $\tilde{q}_{\mathrm{A}i}$ and $\tilde{q}_{\mathrm{s}j}$ are the complex amplitudes of modal displacement of the ABH-DVA and the host structure, respectively.

Solution of Eq. (13) gives:

$$\begin{aligned}\tilde{q}_{\mathrm{A}i} &= \frac{\alpha_{ij}\omega^2}{\Delta}\overline{F}_{\mathrm{m}j},\\ \tilde{q}_{\mathrm{s}j} &= \frac{\omega_{\mathrm{A}i}^2-\omega^2+j2\zeta_{\mathrm{A}}\omega_{\mathrm{A}i}\omega}{\Delta}\overline{F}_{\mathrm{m}j},\end{aligned} \tag{14}$$

where

$$\Delta = \left(\omega_{\mathrm{A}i}^2-\omega^2+j2\zeta_{\mathrm{A}}\omega_{\mathrm{A}i}\omega\right)\left(\omega_{\mathrm{s}j}^2-\omega^2+j2\zeta_{\mathrm{s}}\omega_{\mathrm{s}j}\omega\right)-\alpha_{ij}^2\omega^4. \tag{15}$$

When the coupling coefficient $\alpha_{ij}=0$, the ith mode in the DVA is not coupled with jth structural mode. The amplitude of the structural mode at $\omega=\omega_{\mathrm{s}j}$, at which the real part of the determinant Δ is zero, is usually defined as the resonance amplitude. When the resonance amplitude is normalized with respect to the static displacement δ_{st}, it can be expressed in the following form:

$$\left|\frac{\tilde{q}_{\mathrm{s}j}}{\delta_{\mathrm{st}}}\right| = \frac{1}{2\zeta_{\mathrm{s}}}, \tag{16}$$

where $\delta_{\mathrm{st}}=\overline{F}_{\mathrm{m}j}/\omega_{\mathrm{s}j}^2$.

When $\alpha_{ij}\neq 0$, the complex amplitude of the host structure is:

$$\tilde{q}_{\mathrm{s}j} = \frac{\beta_{ij}^2-\Omega^2+j2\zeta_{\mathrm{A}}\beta_{ij}\Omega}{\left(\beta_{ij}^2-\Omega^2+j2\zeta_{\mathrm{A}}\beta_{ij}\Omega\right)\left(1-\Omega^2+j2\zeta_{\mathrm{s}}\Omega\right)-\alpha_{ij}^2\Omega^4}\delta_{\mathrm{st}}, \tag{17}$$

where $\beta_{ij}=\omega_{\mathrm{A}i}/\omega_{\mathrm{s}j}$ is the frequency ratio and $\Omega=\omega/\omega_{\mathrm{s}j}$ is the normalized frequency.

The denominator in Eq. (17) is the dimensionless form of the determinant Δ. For convenience, the frequencies at which the real part of the denominator becomes zero are defined as the resonance frequencies. That is, the resonance frequencies satisfy:

$$\left(1-\alpha_{ij}^2\right)\Omega^4-\left(\beta_{ij}^2+4\zeta_{\mathrm{A}}\zeta_{\mathrm{s}}\beta_{ij}+1\right)\Omega^2+\beta_{ij}^2=0. \tag{18}$$

The two roots of Eq. (18) is denoted by Ω_1 and Ω_2 ($\Omega_1>\Omega_2$), respectively. Obviously, Ω_k ($k=1,2$) are functions of the frequency ratio β_{ij}. The relationship between Ω_k ($k=1,2$) and β_{ij} with α_{ij} as the parameter is shown in Figure 6(a). It is obvious that one of the two normalized resonance frequencies approaches 1 and the other approaches β_{ij} as β_{ij} deviates significantly from 1. That is, one resonance frequency approaches $\omega_{\mathrm{s}j}$ and the other approaches $\omega_{\mathrm{A}i}$. Additionally, it is worth noting that a larger coupling coefficient allows for a greater tolerance in the coupling frequency. This means that even with slight deviations from the ideal frequency ratio, the damping effect can still be maintained effectively when the coupling coefficient is higher. The larger the coupling coefficient, the more robust the system becomes against variations in the coupling frequency. It indicates that the dynamic interaction between the two modes weakens as β_{ij} deviates from 1.

The normalized modal amplitudes of the structure at these two resonance frequencies are:

$$\left|\frac{\tilde{q}_{\mathrm{s}j}^{(k)}}{\delta_{\mathrm{st}}}\right| = \frac{\sqrt{\left(\beta_{ij}^2-\Omega_k^2\right)^2+\left(2\zeta_{\mathrm{A}}\beta_{ij}\Omega_k\right)^2}}{\left|2\zeta_{\mathrm{s}}\Omega_k\left(\beta_{ij}^2-\Omega_k^2\right)+2\zeta_{\mathrm{A}}\beta_{ij}\Omega_k\left(1-\Omega_k^2\right)\right|}, \quad (k=1,2). \tag{19}$$

Obviously, the normalized modal amplitudes $\left|\tilde{q}_{\mathrm{s}j}^{(k)}\middle/\delta_{\mathrm{st}}\right|$ ($k=1,2$) are functions of β_{ij}. As an example, the damping ratios of ABH-DVA modes and structural modes are set to $\zeta_{\mathrm{A}}=0.1$ and $\zeta_{\mathrm{s}}=0.001$, respectively. Variation of the normalized modal amplitudes as functions of β_{ij} with the coupling coefficient α_{ij} as the parameter is shown in Figure 6(b).

According to Figure 6(b), the normalized amplitude of the peak with lower frequency Ω_2 increases with frequency ratio β_{ij}, and that of the peak with higher frequency degree Ω_1 increases with β_{ij}. To achieve the best performance, the optimal β_{ij} should be located at the crossover point of the two amplitude curves. For $\alpha=0.1$, the optimal value is about $\beta_{ij}=0.99$, and for $\alpha=0.2$, the optimal value is about $\beta_{ij}=0.96$. When the frequency ratio deviates from the optimal value by 10%, the amplitude at one of the peaks becomes almost twice. In order to achieve good damping performance, frequency matching with β_{ij} in the vicinity of the optimal value is very important. Indeed, the density of coupled modes of the ABH-DVA in the frequency domain plays a crucial role in enhancing damping performance. A higher modal density indicates a greater number of modes available for coupling between the DVA and the host structure. This increased modal density leads to a higher probability of modal coupling, facilitating efficient energy transfer and vibration suppression between the two systems. Consequently, a higher modal density contributes to improved damping performance by enabling a broader range of modes to participate in the vibration reduction process.

In order to verify the above statement, the modal frequencies of the P3ABH-DVA, SABH-DVA of equal size and the host plate in Figure 3 are calculated. The frequency range up to 2000 Hz is illustrated in Figure 7. It can be seen that SABH-DVA has many symmetric

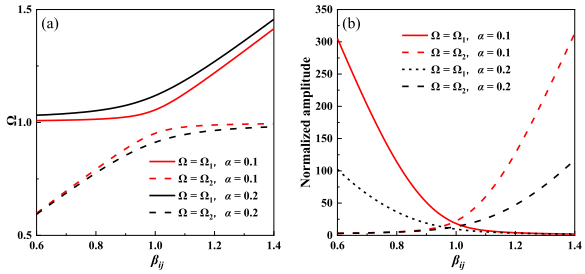

Figure 6 Influence of modal frequency ratio on excitation frequency ratio and normalized amplitude: (**a**) Variation of the normalized frequency with frequency ratio, (**b**) Variation of the normalized amplitude with frequency ratio

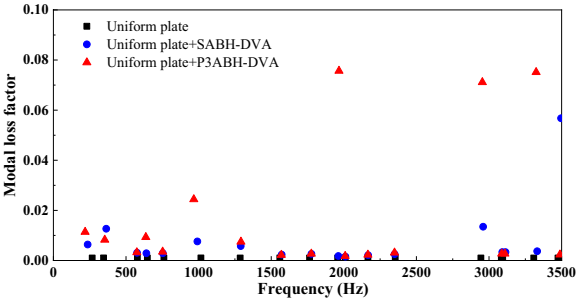

Figure 8 Modal loss factor corresponding to each peak in the response curves

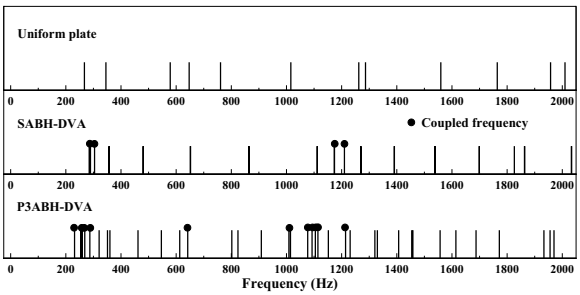

Figure 7 Modal frequency distribution of three structures within 2000 Hz

modes, but few modes can be coupled with the host structure, and the overall mode density and coupled mode density of P3ABH-DVA are significantly higher than that of SABH-DVA, especially during 200–400 Hz and 1000–1200 Hz intervals, which also explains that the response of the system with P3ABH-DVA in Figure 4 is lower than that of the system with SABH-DVA in the above frequency band.

The damping increase brought up by DVAs to the system can also be seen from the response curve (Figure 4). Extracting the typical peaks within 3500 Hz of the three response curves, keeping the same number of peaks of the three curves, the damping of each peak is obtained by simulation and shown in Figure 8. It is obvious that the system with P3ABH-DVA has higher damping ratio and lower response than that with SABH-DVA, as a result of the increase in the coupling caused by the expansion of frequency ratio. In fact, the change of effective mass distribution is also an indispensable account, which will be explained in Section 3.2.

3.2 Mass Effect of DVAs

The mass ratio is another influencing factor of vibration reduction effect. However, it is difficult to understand the mass effect directly from Eq. (12) because it has been normalized with respect to modal mass. Instead, the effective modal mass is considered [33]. It is obvious that the two substructures are coupled through the reacting forces related to the three degrees of freedom (DOFs) at the installation point, which are w_{sn}, θ_{nx} and θ_{ny}, respectively. The modal mass participation factors of the ith ABH-DVA mode related to the three interface DOFs are $\alpha_{i1}^{(k)}(k = 1, 2, 3)$, respectively. The effective modal masses are the square of the modal mass participation factors [33]:

$$M_i^{(k)} = \left(\alpha_{i1}^{(k)}\right)^2 \quad (k = 1, 2, 3). \tag{20}$$

The above expression indicates that the coupling coefficient has included the information of effective modal mass of the ABH-DVA.

The effective modal mass proportion (EMMP) of the ith mode is defined as:

$$R_i^{(k)} = \frac{M_i^{(k)}}{\sum_{i=1}^{\infty} M_i^{(k)}} \quad (k = 1, 2, 3), \tag{21}$$

and the cumulative effective modal mass proportion (CEMMP) below a given frequency f is defined as:

$$\hat{R}_{if}^{(k)} = \frac{\sum_{i=1}^{f_i \le f} M_i^{(k)}}{\sum_{i=1}^{\infty} M_i^{(k)}} \quad (k = 1, 2, 3). \tag{22}$$

As a numerical example, the EMMPs, $R_i^{(k)}$, of the SABH-DVA and P3ABH-DVA in the frequency range below 1500 Hz are shown in Figures 9(a) and (c). The SABH-DVA contains 22 modes and the P3ABH-DVA has 30 modes in the frequency range below 2000 Hz. Obviously, each coupled mode of the P3ABH-DVA has smaller EMMP than that of the SABH-DVA, but the P3ABH-DVA has a larger number

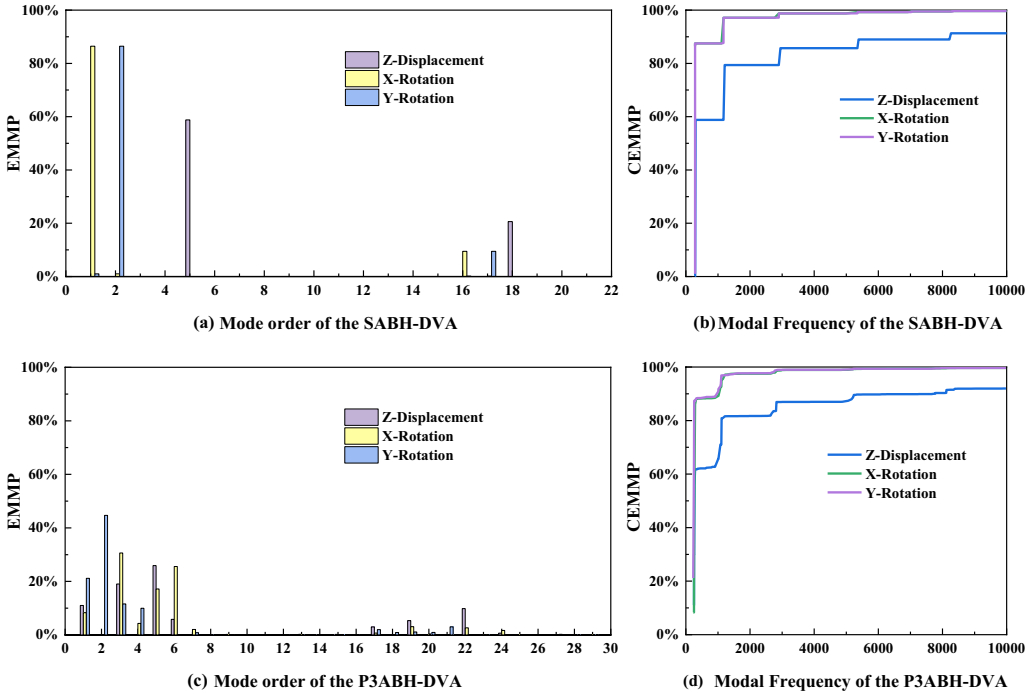

Figure 9 EMMP and CEMMP of the SABH-DVA and P3ABH-DVA

of modes interacting with the host structure than SABH-DVA. The smaller EMMP of the P3ABH-DVA modes can be attributed to the fact that different partitions can vibrate almost independently in the P3ABH-DVA. More interacting modes in the P3ABH-DVA can be attributed to the loss of symmetry in its geometry.

Variations of the cumulative effective modal mass proportion (CEMMP), $\hat{R}_{if}^{(k)}$, of the SABH-DVA and P3ABH-DVA in the frequency range below 10 kHz are shown in Figures 9(b) and (d). It is obvious that although the EMMP of P3ABH-DVA is smaller than that of the SABH-DVA, but its CEMMP is not small, and in some frequency ranges, slightly larger than the SABH-DVA. It means that the effective mass is hardly reduced due to partition the SABH-DVA into three parts in the P3ABH-DVA. On the other hand, more coupled modes in a given frequency range lead to higher modal density and easier frequency matching between the modes of the P3ABH-DVA and those of SABH-DVA.

Based on the above analysis, it is clear that cutting the ABH-DVA into some parts can increase the density of coupled modes and improve the damping effect on more modes of the host structure. Although the 1st, 2nd and 5th modes of the SABH-DVA have very high effective modal mass proportion and they are strongly coupled with most of the modes of the host structure as shown in Figure 5(a), they are only effective for the modes of the host structure below 500 Hz due to the influence frequency ratio. The next strongly coupled modes of the SABH-DVA are the 16th, 17th and 18th modes and the frequency gap is 869.62 Hz, from 304.28 Hz of the 5th to 1173.9 Hz of the 16th mode. The frequency gap for the P3ABH-DVA is 688.14 Hz, from 320.76 Hz of the 7th mode to 1008.9 Hz of the 17th mode, as shown in Figure 5(b). The 11th, 12th and 13th modes of P3ABH-DVA are also weakly coupled. Therefore, the mode of the host structure at 1015.9 Hz can be effectively reduced by the P3ABH-DVA.

4 Other Influencing Factors

Since the analysis in the above section indicates that the damping performance can be improved by partitioning the ABH-DVA into several parts, it is necessary to discuss the influence of the number of slits and the orientation of the partitions.

4.1 Influence of the Number of Slits

As an example, PABH-DVAs of the same size with four and five slits are considered in this section. The partition schemes in these two PABH-DVAs are shown in Figure 10, and the host structure is the same as that in Section 2.1, maintaining the same installation position, external excitation, material parameters, etc.

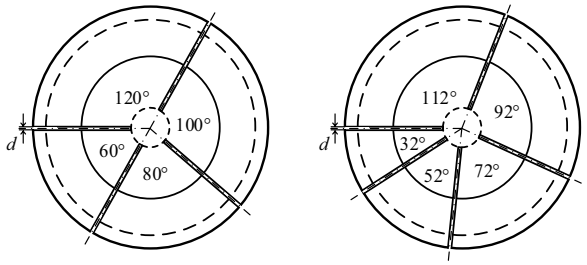

(a) P4ABH-DVA (b) P5ABH-DVA

Figure 10 Other partitioned DVA schemes

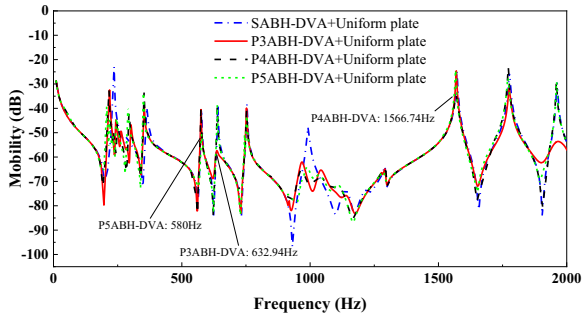

(a) Driving point mobility

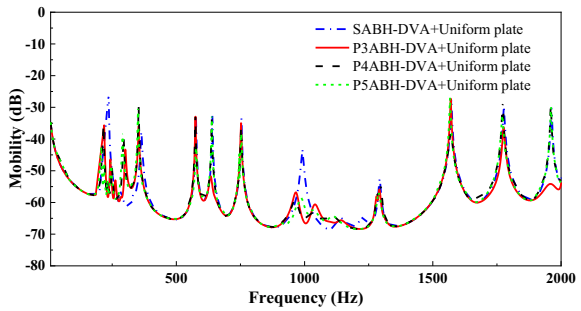

(b) Mean velocity

Figure 11 Driving point mobility and mean velocity of the host plate with other partitioned DVAs

The driving point mobility and mean velocity of synthesized system with different add-on DVAs within 2000 Hz are shown in Figure 11. It can be seen that the DVA with different number of slits can produce better vibration suppression effect than SABH-DVA, and the specific frequency of each type of DVA is different. This can be explained from the mechanism of vibration reduction.

Without loss of generality, the function of the ith mode of the add-on structure in a polar coordinate can be expressed as $\phi_{\mathrm{A}i}(r,\theta)$. The factor $\alpha_{i1}^{(k)}$ $(k=1,2,3)$ in Eq. (11) can be converted into the following form in the continuous space as [33]:

$$\begin{aligned}\alpha_{i1}^{(1)} &= \boldsymbol{\Phi}_{Ai}^{\mathrm{T}}\boldsymbol{M}_A\{1\} = \iint \phi_{\mathrm{A}i}(r,\theta)\rho h(r) r\mathrm{d}r\mathrm{d}\theta,\\ \alpha_{i1}^{(2)} &= \boldsymbol{\Phi}_{Ai}^{\mathrm{T}}\boldsymbol{M}_A\boldsymbol{R}_y = \iint \phi_{\mathrm{A}i}(r,\theta) y\rho h(r) r\mathrm{d}r\mathrm{d}\theta,\\ \alpha_{i1}^{(3)} &= \boldsymbol{\Phi}_{Ai}^{\mathrm{T}}\boldsymbol{M}_A\boldsymbol{R}_x = \iint \phi_{\mathrm{A}i}(r,\theta) x\rho h(r) r\mathrm{d}r\mathrm{d}\theta.\end{aligned} \tag{23}$$

In the symmetrical ABH-DVA, r and θ in $\phi_{\mathrm{A}i}(r,\theta)$ are separable and the mode with a radial order m and a circumferential order n is denoted by RmCn, whose modal function writes:

$$\phi_{\mathrm{A}i}(r,\theta) = \phi'_{\mathrm{A}i}(r)\cos(n\theta+\theta_0). \tag{24}$$

When the axisymmetry of the device is destroyed in the PABH-DVA, $\phi_{\mathrm{A}i}(r,\theta)$ becomes more complex and the r and θ are not separable anymore. Therefore, theoretically $\alpha_{i1}^{(1)}$, $\alpha_{i1}^{(2)}$ and $\alpha_{i1}^{(3)}$ in Eq. (23) do not become zero for any mode number i.

This new configuration preserves the ABH profile in the radial direction alongside a continuous variation along circumferential direction and breaks the axisymmetry of the original DVA design at the same time. The targeted outcome is a compact and light-weight device with enriched ABH features and enhanced coupling with a host structure onto which it is surface-mounted to achieve broadband vibration suppressions without a complex tuning procedure.

4.2 Influence of Installation Angle

In order to investigate the influence of installation angle, a 65° partition from the P3ABH-DVA is considered. Two cases (I and II), 180° different, are shown in Figure 12. The mobility of the two cases are shown in Figure 13.

It is obvious from Figure 13 that Case II has a better vibration suppression effect than Case I, especially at 267 Hz, 653 Hz and 1015 Hz in the lower frequency range, while the damping effect of the two cases being almost the same at higher frequency range. The reason is that the coupling coefficient is different in the two cases. According to Eq. (14), the damping effect of ABH-DVAs depends on the coupling coefficient, which is expressed as the product of $\alpha_{i1}^{(k)}(k=1,2,3)$ and $\alpha_{j2}^{(k)}(k=1,2,3)$, as shown in Eqs. (10) and (11). As discussed above, $\alpha_{i1}^{(k)}(k=1,2,3)$ contains the modal information of the ABH-DVA and $\alpha_{j2}^{(k)}(k=1,2,3)$ depends on the installation position of the ABH-DVA on the host structure.

In order to explain the observed differences of damping effect in relation to the installation angle, the corresponding coupling coefficients are considered. The only difference in Case I and Case II is that the ABH

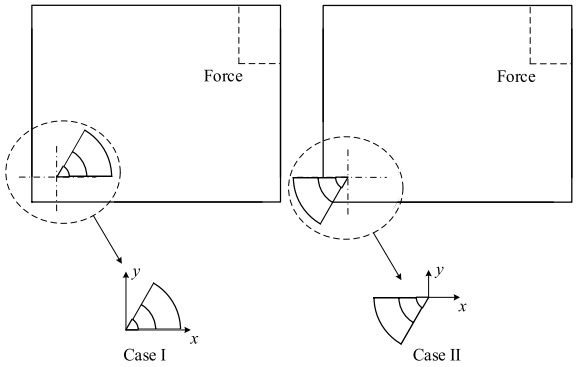

Figure 12 Different installation angle schemes of DVA

has been rotated by 180°. It means that there exist $\phi_{\mathrm{A}i}^{\mathrm{I}}(r,\theta)=\phi_{\mathrm{A}i}^{\mathrm{II}}(r,\theta+\pi)$ and $h^{\mathrm{I}}(r,\theta)=h^{\mathrm{II}}(r,\theta+\pi)$, in which $\phi_{\mathrm{A}i}^{\mathrm{I}}(r,\theta)$ and $\phi_{\mathrm{A}i}^{\mathrm{II}}(r,\theta)$ are the modal functions of the DVAs in Case I and Case II, respectively, and $h^{\mathrm{I}}(r,\theta)$ and $h^{\mathrm{II}}(r,\theta)$ are the thickness of the two DVAs. $\alpha_{j2}^{(k)}(k=1,2,3)$ are the same for the two cases because they have the same installation position. As shown in Ref. [30], $\alpha_{i1}^{(1)}$ of Eq. (11) in an equivalent continuous system can be written as:

$$\begin{aligned}\alpha_{i1}^{(1)(\mathrm{II})}&=\int_0^R\int_0^{2\pi}\phi_{\mathrm{A}i}^{\mathrm{II}}(r,\theta)\rho h^{\mathrm{II}}(r,\theta)r\mathrm{d}r\mathrm{d}\theta\\&=\int_0^R\int_{-\pi}^{\pi}\phi_{\mathrm{A}i}^{\mathrm{II}}(r,\theta+\pi)\rho h^{\mathrm{II}}(r,\theta+\pi)r\mathrm{d}r\mathrm{d}\theta\\&=\int_0^R\int_0^{2\pi}\phi_{\mathrm{A}i}^{\mathrm{I}}(r,\theta)\rho h^{\mathrm{I}}(r)r\mathrm{d}r\mathrm{d}\theta=\alpha_{i1}^{(1)(\mathrm{I})},\end{aligned}\tag{25}$$

where $\alpha_{i1}^{(1)(\mathrm{I})}$ and $\alpha_{i1}^{(1)(\mathrm{II})}$ are the coefficients of Case I and Case II, $\alpha_{i1}^{(2)}$ can be written as:

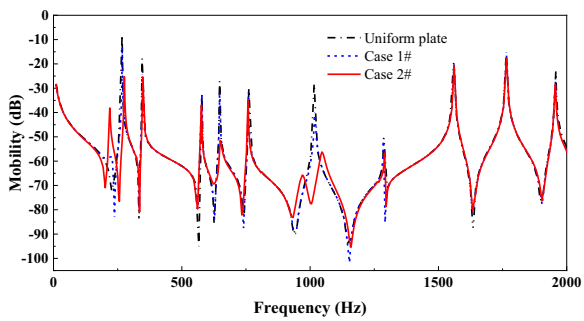

Figure 13 Driving point mobility of the host plate with different installation angle DVAs

$$\begin{aligned}\alpha_{i1}^{(2)(\mathrm{II})}&=\int_0^R\int_0^{2\pi}\phi_{\mathrm{A}i}^{\mathrm{II}}(r,\theta)\rho h^{\mathrm{II}}(r,\theta)r^2\sin\theta\mathrm{d}r\mathrm{d}\theta\\&=\int_0^R\int_{-\pi}^{\pi}\phi_{\mathrm{A}i}^{\mathrm{II}}(r,\theta+\pi)\rho h^{\mathrm{II}}(r,\theta+\pi)r^2\sin(\theta+\pi)\mathrm{d}r\mathrm{d}\theta\\&=-\int_0^R\int_0^{2\pi}\phi_{\mathrm{A}i}^{\mathrm{I}}(r,\theta)\rho h^{\mathrm{I}}(r)r^2\sin\theta\mathrm{d}r\mathrm{d}\theta=-\alpha_{i1}^{(2)(\mathrm{I})}.\end{aligned}\tag{26}$$

Similarly, there exists:

$$\alpha_{i1}^{(3)(\mathrm{II})}=-\alpha_{i1}^{(3)(\mathrm{I})}.\tag{27}$$

The above results indicate:

$$\alpha_{ij}^{(\mathrm{I})}=\alpha_{i1}^{(1)(\mathrm{I})}\alpha_{j2}^{(1)}+\alpha_{i1}^{(2)(\mathrm{I})}\alpha_{j2}^{(2)}+\alpha_{i1}^{(3)(\mathrm{I})}\alpha_{j2}^{(3)},\tag{28}$$

$$\alpha_{ij}^{(\mathrm{II})}=\alpha_{i1}^{(1)(\mathrm{I})}\alpha_{j2}^{(1)}-\alpha_{i1}^{(2)(\mathrm{I})}\alpha_{j2}^{(2)}-\alpha_{i1}^{(3)(\mathrm{I})}\alpha_{j2}^{(3)}.\tag{29}$$

The damping of the first two structural modes of the host structure is considered. Their respective frequencies are 267.41 Hz and 345.41 Hz, and their modal shapes are shown in Figures 14(a) and (b). The corresponding natural frequencies of the 65°-partition DVA are 228.86 Hz and 320.23 Hz and their modal shapes are shown in Figures 14(c)−(f). Obviously, there exists $\phi_{\mathrm{A}i}^{\mathrm{I}}(r,\theta)=\phi_{\mathrm{A}i}^{\mathrm{II}}(r,\theta+\pi)$ for the modal shape of the partitioned DVAs in two cases. The frequency ratios are $\beta_{11}=0.856$ and $\beta_{22}=0.927$, respectively.

The three terms on the right side of Eq. (28), $\alpha_{ij}^{(k)}=\alpha_{i1}^{(k)}\alpha_{j2}^{(k)}$ $(k=1,2,3)$, are calculated and their values for the two cases are shown in Table 3. For the interaction between the 1st structural mode and 1st DVA mode, their coupling coefficients are $\alpha_{11}^{(\mathrm{I})}=0.0593$ and $\alpha_{11}^{(\mathrm{II})}=0.1945$, respectively for Case I and Case II. Apparently, Case II has a larger coupling coefficient than Case I due to the cancellation of different terms in Eq. (28) and Eq. (29) for Case I. The first two peaks in the coupled system are ω_2=219.09 Hz and ω_1=276.21 Hz. This can also explain that the dynamic vibration absorption effect of Case II is much better than Case I. Since $\beta_{11}=0.856$ is significantly smaller than its optimal value (more than 10%), there exist $\Omega_2=0.819\approx\beta_{11}$ and $\Omega_1=1.045\approx1$, which is in agreement with the result in Figure 6(a). Figure 13 shows that the peak at ω_1=267.86 Hz is less significantly reduced, which also agrees with the result in Figure 6(b). Since $\alpha_{11}^{(\mathrm{II})}>\alpha_{11}^{(\mathrm{I})}$, the peak at ω_1 of Case II is smaller than that of Case I, which is also consistent with Figure 6(b). This also indicates that the installation angle can also influence the damping performance. For the modes at 267 Hz, 653 Hz and 1015 Hz shown

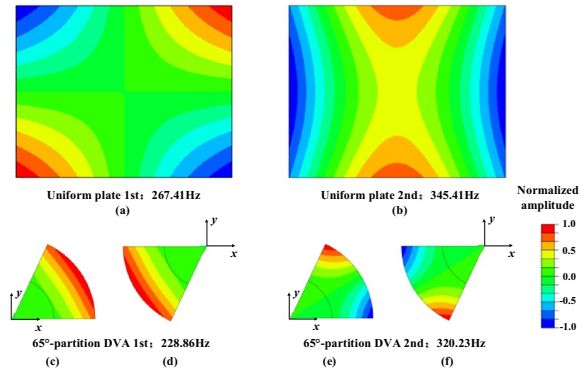

Figure 14 Modal shape of the two different installation angle cases: (**a**) The 1st mode of host plate, (**b**) The 2nd mode of host plate, (**c**) The 1st mode of 65°-partition DVA in case I, (**d**) The 1st mode of 65°-partition DVA in case II, (**e**) The 2nd mode of 65°-partition DVA in case I, (**f**) The 2nd mode of 65°-partition DVA in case II

Table 3 Coupling sequences and coupling coefficients at different installation angles

Coupling sequence	i	j	$\alpha_{ij}^{(1)}=\alpha_{i1}^{(1)}\alpha_{j2}^{(1)}$	$\alpha_{ij}^{(2)}=\alpha_{i1}^{(2)}\alpha_{j2}^{(2)}$	$\alpha_{ij}^{(3)}=\alpha_{i2}^{(3)}\alpha_{j2}^{(3)}$
Case I (Figures 14(c), (a))	1	1	0.1269	−0.0332	−0.0344
Case II (Figures 14(d), (a))			0.1269	0.0332	0.0344
Case I (Figures 14(e), (b))	2	2	0	−0.0082	−0.0180
Case II (Figures 14(f), (b))			0	0.0082	0.0180

in Figure 13, Case II yields better vibration suppression effect than Case I.

For the interaction between the 2nd structural mode and 2nd DVA mode, there exist $\alpha_{22}^{(\mathrm{I})}=-0.0262$ and $\alpha_{22}^{(\mathrm{II})}=0.0262$. Since the coupling coefficient α_{ij} appears in the determinant Δ (Eq. (15)) in the squared form, its sign does affect the damping performance. Since $\beta_{22}=0.927$ and $|\alpha_{22}|=0.0262$ are both relatively small, ω_1=347.53 Hz and $\Omega_1=1.006\approx 1$. The small value of $|\alpha_{22}|=0.0262$ indicates a weak interaction between the host structure and the DVA. The weak interaction leads to the result that the peak at ω_1=347.53 Hz is only slightly reduced and the other peak is not clearly visible in the frequency response curve in Figure 13.

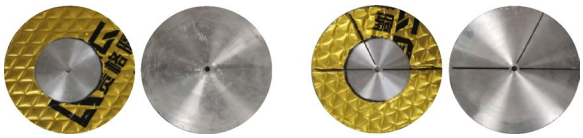

Figure 15 Experimental object of SABH-DVA and P3ABH-DVA

5 Experimental Verifications

Experiments were carried out to verify the above broadband vibration suppression phenomenon. The DVAs and the host plate utilized for comparison were produced by aluminum using computer numerical control (CNC) milling. The add-on DVAs were attached onto the host structure using a standard 5 mm screw, as shown in Figure 15, the size and damping substance were identical to those of the simulations mentioned above.

Figure 16 shows the experimental setup. An electromagnetic shaker (B&K 4809), driven by a power amplifier (B&K 2718), was used to generate a periodic chirp force from 10 Hz to 3500 Hz to excite the plate at the position in the above simulation. The free boundary condition in the experiment was achieved by suspending the plate to a rigid frame using two elastic strings. A Polytec™ Laser Scanning Vibrometer (PSV 500) was used to perform the response measurement.

The driving point mobility and the mean velocity of the host structure and synthetic systems were measured up to 3500 Hz and the results are shown in Figure 17. The response curves of the two DVAs basically reflects the two main vibration suppression mechanisms of conventional DVA effect (about 260 Hz) and energy dissipation (about 600 Hz). Besides, it can be observed that the P3ABH-DVA generally leads to the best control performance, in terms of both resonant peak attenuation and broadband vibration reduction, such as 259 Hz, 1020 Hz and 2204 Hz, there are 21 dB, 8 dB and 7 dB attenuation respectively. As demonstrated in numerical simulations, this is owing to the partitioned DVA changes the effective mass distribution by sacrificing a small amount of effective modal mass, brings more modal frequencies and increases the coupling opportunities with the host plate. The coupling coefficients in some specific frequency bands is also increases, collectively contributes to a broadband vibration reduction of the system. Although there are some inevitable errors in the experiment, the overall trend is consistent with the above simulation.

In addition, the partitioned DVA still maintains some basic characteristics of the symmetrical DVA, it cannot guarantee that all frequency bands can achieve excellent vibration reduction effect. This has also been confirmed in the simulation. If multi-band vibration reduction is

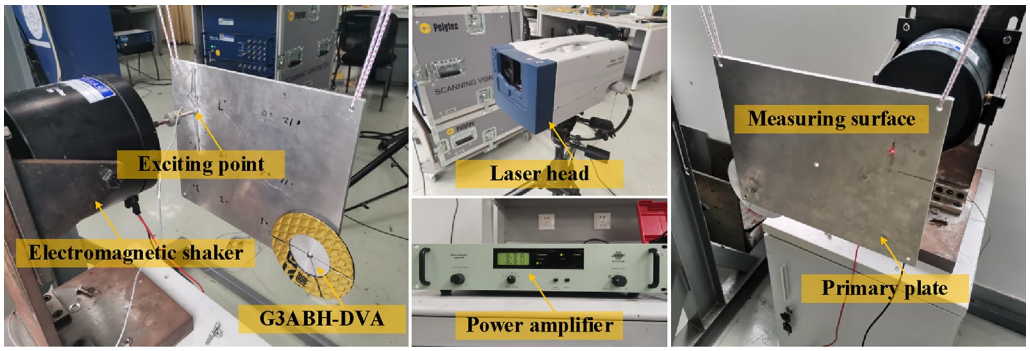

Figure 16 Experimental test set-up

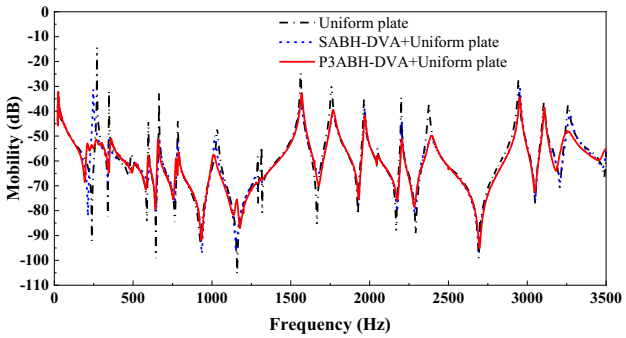

Figure 17 Experimentally measured vibration responses of the host plate without and with different DVAs: (**a**) Driving point mobility, (**b**) Mean velocity of plate surface

required, the deficiency at some specific frequencies can be alleviated by adjusting the slits, increasing the number of DVAs or adopting other ways to break the symmetry.

6 Conclusions

This paper proposes a partitioned ABH-based dynamic vibration absorber (abbreviated as PABH-DVA), as an auxiliary add-on device for the vibration reduction in a controlled structure. The proposed configuration retains the basic ABH profile, thus preserving the energy focalization ability in each cut segment of the disc. The main conclusions are drawn as follows.

(1) The new PABH-DVA yields better damping performing than the original symmetric ABH-DVA. The underlying mechanism of this phenomenon roots in the frequency relationship between the two structures (frequency ratio) and the modal participation factor (mass ratio).
(2) The proposed PABH-DVA improves the coupling characteristics with the host structure by changing the frequency ratio. It increases its modal density by cutting slits to improve the chance of coupling with the vibration modes of the host structure, so as to improve the vibration suppression performance. The slit position of the add-on DVA does not show much influence thus needing no particular optimization, which is an advantage of the PABH-DVA.
(3) The proposed PABH-DVA improves the coupling characteristics with the host structure by enriching the mass ratio. Although each of the coupled modes of PABH-DVA has a smaller effective modal mass proportion than SABH-DVA, the number of modes that PABH-DVA interacts with the host structure is greater than that of SABH-DVA. The total cumulative effective modal mass proportion is not small and is slightly larger than SABH-DVA in some frequency ranges. Theoretically, increasing the number of slits is beneficial to frequency matching, but it also sacrifices the modal effective mass. Therefore, although the number or position of slots does not need to be precisely designed, a certain trade-off needs to be made in light of the characteristics of the structure to be controlled.
(4) Other influencing factors, the installation angles have also been considered. Different installation

angles can cause differences in some specific peaks. Therefore, ensuring that the coupling coefficients in three directions to play a positive role is important when considering the installation angle.

All in all, this study details and reveals the coupling mechanism between the DVA and the host structure. The study is expected to generate new impetus for the exploration of practical engineering application of ABH-based technology.

Acknowledgements
Not applicable.

Authors' Contributions
HJ and JQ was in charge of the whole trial; XZ wrote the manuscript; CW assisted with the result analysis; LC assisted with sampling and laboratory analyses. All authors read and approved the final manuscript.

Funding
Supported by National Key Research and Development Program of China (Grant No. 2021YFB3400100) and National Natural Science Foundation of China (Grant Nos. 52241103, U2241261, 52022039).

Declarations

Competing Interests
The authors declare no competing financial interests.

Received: 28 September 2022 Revised: 12 May 2024 Accepted: 29 May 2024
Published online: 23 July 2024

References

[1] X Shan, Y Li, H Liu, et al. Residual vibration reduction of high-speed pick-and-place parallel robot using input Shaping. *Chinese Journal of Mechanical Engineering*, 2022, 35: 16. https://doi.org/10.1186/s10033-022-00679-3.
[2] Y Wu, S Li, K Fan, et al, Investigation of an ultra-low frequency piezoelectric energy harvester with high frequency up-conversion factor caused by internal resonance mechanism. *Mechanical Systems and Signal Processing*, 2022, 162: 108038. https://doi.org/10.1016/j.ymssp.2021.108038.
[3] V V Krylov, F J B S Tilman. Acoustic 'black holes' for flexural waves as effective vibration dampers. *Journal of Sound and Vibration*, 2004, 274(3): 605–619. https://doi.org/10.1016/j.jsv.2003.05.010.
[4] V V Krylov. New type of vibration dampers utilising the effect of acoustic 'black holes'. *Acta Acustica united with Acustica*, 2004, 90: 830–837. https://www.researchgate.net/publication/233521336.
[5] V B Georgiev, J Cuenca, F Gautier, et al. Damping of structural vibrations in beams and elliptical plates using the acoustic black hole effect. *Journal of Sound and Vibration*, 2011, 330(11): 2497-2508. https://doi.org/10.1016/j.jsv.2010.12.001.
[6] J Cheer, K Hook, S Daley. Active feedforward control of flexural waves in an Acoustic Black Hole terminated beam. *Smart Materials and Structures*, 2021, 30(3): 035003. https://doi.org/10.1088/1361-665X/abd90f.
[7] W Huang, H Ji, J Qiu, et al. Wave energy focalization in a plate with imperfect two-dimensional acoustic black hole indentation. *Journal of Vibration and Acoustics*, 2016, 138(6). https://doi.org/10.1115/1.4034080.
[8] J Leng, V Romero-García, A Pelat, et al. Interpretation of the Acoustic Black Hole effect based on the concept of critical coupling. *Journal of Sound and Vibration*, 2020, 471: 115199. https://doi.org/10.1016/j.jsv.2020.115199.
[9] V V Krylov, R E T B Winward. Experimental investigation of the acoustic black hole effect for flexural waves in tapered plates. *Journal of Sound and Vibration*, 2007, 300(1): 43–49. https://doi.org/10.1016/j.jsv.2006.07.035.
[10] V Kralovic, V V Krylov. Damping of flexural vibrations in tapered rods of power-law profile: Experimental studies. *Proceedings of the Institute of Acoustics*, 2007, 29: 66–73. https://www.researchgate.net/publication/281976853.
[11] E P Bowyer, D J O'Boy, V V Krylov, et al. Experimental investigation of damping flexural vibrations in plates containing tapered indentations of power-law profile. *Applied Acoustics*, 2013, 74(4): 553–560. https://doi.org/10.1016/j.apacoust.2012.10.004.
[12] P A Feurtado, S C Conlon. An experimental investigation of acoustic black hole dynamics at low, mid, and high frequencies. *Journal of Vibration and Acoustics*, 2016, 138(6). https://doi.org/10.1115/1.4033894.
[13] L Tang, L Cheng, H Ji, et al. Characterization of acoustic black hole effect using a one-dimensional fully-coupled and wavelet-decomposed semi-analytical model. *Journal of Sound and Vibration*, 2016, 374: 172–184. https://doi.org/10.1016/j.jsv.2016.03.031.
[14] J J Bayod. Experimental study of vibration damping in a modified elastic wedge of power-law profile. *Journal of Vibration and Acoustics*, 2011, 133(6). https://doi.org/10.1115/1.4003591.
[15] S C Conlon, J B Fahnline, F Semperlotti. Numerical analysis of the vibroacoustic properties of plates with embedded grids of acoustic black holes. *The Journal of the Acoustical Society of America*, 2015, 137(1): 447–457. https://doi.org/10.1121/1.4904501.
[16] N Gao, Z Wei, H Hou, et al. Design and experimental investigation of V-folded beams with acoustic black hole indentations. *Journal of the Acoustical Society of America*, 2019, 145(1): EL79–EL83. https://doi.org/10.1121/1.5088027.
[17] J Deng, L Zheng, P Zeng, et al. Passive constrained viscoelastic layers to improve the efficiency of truncated acoustic black holes in beams. *Mechanical Systems and Signal Processing*, 2019, 118: 461–476. https://doi.org/10.1016/j.ymssp.2018.08.053.
[18] M R Shepherd, C A McCormick, S C Conlon, et al. Modeling and optimization of acoustic black hole vibration absorbers. *Journal of the Acoustical Society of America*, 2017, 141(5): 4034–4034. https://doi.org/10.1121/1.4989305.
[19] C A McCormick, M R Shepherd. Design optimization and performance comparison of three styles of one-dimensional acoustic black hole vibration absorbers. *Journal of Sound and Vibration*, 2020, 470: 115164. https://doi.org/10.1016/j.jsv.2019.115164.
[20] L Ma, H Dong, L Cheng. An alternative and optimized thickness profile of an acoustic black hole plate. *Journal of Sound and Vibration*, 2020, 486: 115619. https://doi.org/10.1016/j.jsv.2020.115619.
[21] E P Bowyer, V V Krylov. Experimental investigation of damping flexural vibrations in glass fibre composite plates containing one- and two-dimensional acoustic black holes. *Composite Structures*, 2014, 107: 406–415. https://doi.org/10.1016/j.compstruct.2013.08.011.
[22] E P Bowyer, V V Krylov. Experimental study of sound radiation by plates containing circular indentations of power-law profile. *Applied Acoustics*, 2015, 88: 30–37. https://doi.org/10.1016/j.apacoust.2014.07.014.
[23] E P Bowyer, V V Krylov. A review of experimental investigations into the acoustic black hole effect and its applications for reduction of flexural vibrations and structure-borne sound. *Inter-Noise*, San Francisco, USA, August 9-12, 2015. https://www.researchgate.net/publication/282186765.
[24] L Zhao, S Conlon, F Semperlotti. Broadband energy harvesting using acoustic black hole structural tailoring. *Smart Materials and Structures*, 2014, 23: 065021. https://doi.org/10.1088/0964-1726/23/6/065021.
[25] L Zhao. Passive vibration control based on embedded acoustic black holes. *Journal of Vibration and Acoustics*, 2016, 138(4). https://doi.org/10.1115/1.4033263.
[26] A Pelat, F Gautier, S C Conlon, et al. The acoustic black hole: A review of theory and applications. *Journal of Sound and Vibration*, 2020, 476: 115316. https://doi.org/10.1016/j.jsv.2020.115316.
[27] C Zhao, M G Prasad. Acoustic black holes in structural design for vibration and noise control. *Acoustics*, 2019, 1: 220–251. https://doi.org/10.3390/acoustics1010014.
[28] T Zhou, L Cheng. A resonant beam damper tailored with Acoustic Black Hole features for broadband vibration reduction. *Journal of Sound and Vibration*, 2018, 430: 174–184. https://doi.org/10.1016/j.jsv.2018.05.047.
[29] H Ji, N Wang, C Zhang, et al. A vibration absorber based on two-dimensional acoustic black holes. *Journal of Sound and Vibration*, 2021, 500: 116024. https://doi.org/10.1016/j.jsv.2021.116024.

[30] H Ji, X Zhao, N Wang, et al. A circular eccentric vibration absorber with circumferentially graded acoustic black hole features. *Journal of Vibration and Acoustics*, 2022, 144(2). https://doi.org/10.1115/1.4053475
[31] T Zhou, L Cheng. Planar swirl-shaped acoustic black hole absorbers for multi-directional vibration suppression. *Journal of Sound and Vibration*, 2022, 516: 116500. https://doi.org/10.1016/j.jsv.2021.116500
[32] S Park, J Y Lee, W Jeon. Vibration damping of plates using waveguide absorbers based on spiral acoustic black holes. *Journal of Sound and Vibration*, 2022, 521: 116685. https://doi.org/10.1016/j.jsv.2021.116685
[33] J Wijker. *Spacecraft structures*. Berlin: Springer-Verlag, 2008. https://doi.org/10.1007/978-3-540-75553-1.

Xiaoning Zhao born in 1998, is currently a master candidate at *State Key Laboratory of Mechanics and Control of Mechanical Structures, Nanjing University of Aeronautics and Astronautics, China*.

Chaoyan Wang born in 1984, is currently a researcher at *Nanjing Institute of Information Technology, China*. His main research interests include vibration and noise control, intelligent structures and piezoelectric materials.

Hongli Ji born in 1983, is currently a professor and a PhD candidate supervisor at *State Key Laboratory of Mechanics and Control of Mechanical Structures, Nanjing University of Aeronautics and Astronautics, China*. Her main research interests include vibration and noise control, semi-active control and intelligent structures.

Jinhao Qiu born in 1963, is currently a professor and a PhD candidate supervisor at *State Key Laboratory of Mechanics and Control of Mechanical Structures, Nanjing University of Aeronautics and Astronautics, China*. His main research interests include vibration and noise control, intelligent structures and piezoelectric materials.

Li Cheng is currently a professor and a PhD candidate supervisor at *Department of Mechanical Engineering, Hong Kong Polytechnic University, China*. His main research interests include vibration and noise control, fluid-structure interaction, damage detection.